International Journal of Heat and Mass Transfer 236 (2025) 126256

Contents lists available at ScienceDirect

International Journal of Heat and Mass Transfer

journal homepage: www.elsevier.com/locate/ijhmt

Study of the thermal measurement depth of a skin calorimeter using simple RC and TF models

Pedro Jesús Rodríguez de Rivera [a,*], Miriam Rodríguez de Rivera [b], Fabiola Socorro [a], Manuel Rodríguez de Rivera [a]

[a] *Department of Physics. University of Las Palmas de Gran Canaria. Las Palmas de Gran Canaria, Spain*
[b] *Cardiology Service. Hospital Universitario Marqués de Valdecilla. Santander, Spain*

ARTICLE INFO

Keywords:
Direct calorimetry
Skin heat flux
Skin heat capacity
Skin thermal conductance
Thermal probing depth
Thermal penetration depth

ABSTRACT

An experimental and theoretical study of the heat capacity thermal measurement depth of a skin calorimeter has been carried out. This calorimeter consists of a thermopile placed between a thermostat and an aluminum measuring plate, which is placed on the sample to be measured. We performed simulations using the finite element method (FEM) with inert samples of different sizes. From these simulations, Transfer Functions (TFs) between the calorimeter's thermostat temperature and the temperature of the measuring plate were determined. Compact thermal models (RC models) able to determine the heat capacity of the sample were also determined. We conclude that, in the case of heat-conducting materials, a single time constant is enough to represent the TF. However, at least two time constants are required for heat-insulating materials. In this work we also studied the time dependence of the thermal measurement depth, concluding that this dependence is exponential. Finally, we present some experimental measurements performed on inert samples and on human skin, which are coherent with the results of the simulation.

1. Introduction

The study of human body's thermoregulation is of great interest in medical practice. Heat flux, and especially the temperature, are the two most relevant quantities. The heat flux dissipated by the human body is of great interest when designing air conditioning installations. This heat flux can be determined by direct calorimetry [1]. This technique requires a calorimetric chamber whose installation is complex and currently is not used. The heat flux of an individual is related with his/her metabolism and physical activity, and its study is of interest in different areas of medicine such as cardiology, pneumology, nutrition, sports medicine, etc. To determine a human's energy output, the most accepted technique nowadays is indirect calorimetry. This technique allows the determination of the metabolic equivalent (MET's) from the measurement of the VO_2 consumed by a person. This method is used in subjects at rest and during physical activity. This measurement is relevant both as a function of time and as a peak VO_{2max} value [2].

These heat flux measurements are global, but localized heat flux measurements are also of interest. For this purpose, a calorimetric sensor, also called a skin calorimeter, has been developed. Its main objective is to measure the power dissipated by a 2 × 2 cm^2 skin area [3]. This device has a thermostat whose temperature is programmable, which is a novelty compared to other heat flux sensors [4]. Thus, the power measured depends mainly on the temperature of the thermostat and the physical conditions of the subject. This instrument is of great interest for measuring in skin areas whose dissipation varies significantly with physical exercise.

On the other hand, remote and contact sensors have also been developed to determine the thermal properties of the skin [5,6]. The operation of these sensors is usually the same: the sensor's transient response is studied, as a result of a thermal excitation induced on the skin. In our skin calorimeter, this thermal excitation is performed by programming the device's thermostat temperature. This allows the determination of the thermal resistance and the heat capacity of the skin area where the sensor is applied [7]. This technique has been recently used to study the temporal evolution of small skin lesions [8].

In a previous work, we performed an experimental study of the thermal measurement depth of this sensor [9]. In that work, a simulation to study more cases (that experimentally would require a large amount of time and in some cases, are difficult to perform) was desired. In this paper, we simulate the operation of the calorimeter using the finite

---

* Corresponding author at: Department of Physics. University of Las Palmas de Gran Canaria. Las Palmas de Gran Canaria. Spain.
E-mail address: pedro.rguezderivera@ulpgc.es (P.J. Rodríguez de Rivera).

https://doi.org/10.1016/j.ijheatmasstransfer.2024.126256
Received 22 June 2024; Received in revised form 18 September 2024; Accepted 23 September 2024

Nomenclature

T_{input}	input FT temperature [°C]
T_{output}	output FT temperature [°C]
t	time [s]
t_m	measurement time [s]
m	mass [g]
L	sample thickness [mm]
ω	angular frequency [rad s^{-1}]
f	frequency [Hz]
s	Laplace variable
TF	Transfer Function
$TF(i\omega)$	…in Fourier domain
$TF(s)$	…in Laplace domain
s_i	transfer function pole [s^{-1}]
s_i^*	transfer function zero [s^{-1}]
K	transfer function sensitivity
τ	time constant [s]
τ_i	… $\tau_i = -1/s_i$ (pole value)
τ_i^*	… $\tau_i^* = -1/s_i^*$ (zero value)
ε	temperature fitting root mean square error [°C]
$T_{FEM}[i]$	FEM simulation temperature [°C]
$T_{TF}[i]$	TF model temperature [°C]
n_p	number of points used in the fitting
C_i	heat capacity of element i [J/K]
P_i, P_{ik}	thermal conductance between domains [mW/K]

(nomenclature for all models, 1: conductive sample, 2: insulating sample & 3: device experimental model)

$\boldsymbol{T_{therm}}$	thermostat temperature **[°C]**
$\boldsymbol{T_{plate}}$	measurement plate temperature **[°C]**
$\boldsymbol{T_{room}}$	ambient temperature **[°C]**
$\boldsymbol{T_1}$	sample temperature **[°C]**
$\boldsymbol{C_1}$	…measured, $\boldsymbol{C_1 = C_0 + C_{(sample)}}$
$\boldsymbol{C_0}$	…measurement offset value
$\boldsymbol{P_1}$	…between sample & environment
$\boldsymbol{P_{therm}}$	…between a domain & thermostat

(nomenclature for model 2)

$\boldsymbol{C_{plate}}$	…of the measurement plate
$\boldsymbol{P_{12}}$	…between sample & measuring plate
$\boldsymbol{P_2}$	…between measuring plate & environment

(nomenclature for model 3)

$\boldsymbol{T_0}$	Ambient temperature around the calorimeter **[°C]**
$\boldsymbol{T_{cold}}$	skin calorimeter cold temperature **[°C]**
$\boldsymbol{W_1}$	calibration base dissipated power **[W]**
$\boldsymbol{W_2}$	skin calorimeter thermostat power **[W]**
$\boldsymbol{y}$	skin calorimeter calorimetric signal **[V]**
$\boldsymbol{k}$	thermopile Seebeck coefficient **[V/K]**
$\boldsymbol{C_{therm}}$	…of the calorimeter thermostat
$\boldsymbol{C_{brass}}$	… of brass sample
$\boldsymbol{C_{PTFE}}$	… of PTFE sample
$\boldsymbol{P_{cold}}$	…between thermostat & cooling system

element method to solve the differential equation of heat conduction [10] and determine the temperature at every point at any instant. To determine the heat capacity, we need to know the transient response of the measuring plate temperature, when a thermal excitation is performed on the calorimeter's thermostat. The determination of the transfer function between these temperatures allows the estimation of the complexity of the model that allows the determination of the heat capacity of the sample. The objective of this work is to study the thermal measurement depth of the skin calorimeter for the determination of the heat capacity of the sample. Thermal measurement depth is also of interest in other applications, for example cooling by magnetocaloric effect [11].

In this article, we provide a brief description of the skin calorimeter. Then, a skin calorimeter finite element model is proposed, which allows the determination the temperature temporal variation at every point of every element, when a thermostat temperature change is programmed. Once the geometry, boundary conditions and thermal properties of each domain are defined, the transient heat conduction equation [10] is solved numerically using the finite element method (FEM) [12]. Then, the measuring plate temperature time responses are related with the thermostat temperature. This relationship consists of a one or two-pole Transfer Function (TF), depending on if the sample material is conductive or insulating. A compact thermal model is proposed to determine the heat capacity of the simple. This model allows to study the dependence of the heat capacity obtained with the size of the sample and with the measurement time. Finally, some experimental measurements performed on inert samples and on human skin are shown.

2. Experimental setup

The skin calorimeter consists of a measuring thermopile (13.2 × 13.2 × 2.2 mm, Module ET20–65-F2A-1312–11-W2.25, by Laird) placed between an aluminum measuring plate (20×20×1 mm) and a small aluminum block (14×14×4 mm) that operates as a thermostat. This thermostat contains a heating resistor and a Pt-100 temperature sensor. A cooling system composed by another thermopile (Module ET20–65-F2A-1312–11-W2.25, by Laird), an aluminum heatsink and a fan is attached to the thermostat. The thermal interface between the components is crucial for the precise operation of the instrument. To improve thermal contact, a thin layer of high thermal conductivity thermal paste was applied between the components. Excess paste was removed during assembly by tightening the screws, which ensured proper contact between the parts.

The calibration base consists of an expanded polystyrene (EPS) block. This calibration base has an aluminum block that contains a resistor and a temperature sensor, that allows the calibration of the skin calorimeter when the device is placed on it. The calibration of the calorimeter is performed at different temperatures and powers. Fig. 1 shows each part of the calorimeter. A triple power supply (E3631A, by Keysight) powers all the heating resistors of the calorimeter and the calibration base and the cooling thermopile.

A data acquisition system (34970A with 34901, by Keysight) reads the calorimetric signal from the measurement thermopile, the thermostat temperature, the calibration element temperature and the room temperature. A program written in C++ controls the instrumentation, that is connected to a laptop via the GPIB interface (82357B, by Keysight). The sampling period used in the control of the instrumentation is 0.5 s.

3. Simulation

The goal is to solve the transient heat conduction equation [10] at all points in the spatial domains of the sensor, sample and surroundings (Fig. 2). To solve this equation numerically with the finite element method (FEM) we used the Partial Differential Equation Toolbox of MatLab [12]. This tool allows us to discretize all the domains incorporating the dimensions, densities, specific heat capacities and thermal conductivities of each domain that compose the sensor, the sample and the surroundings. Table 1 shows the thermal properties of each domain considered in the 2D-model-simulation. The program allows the

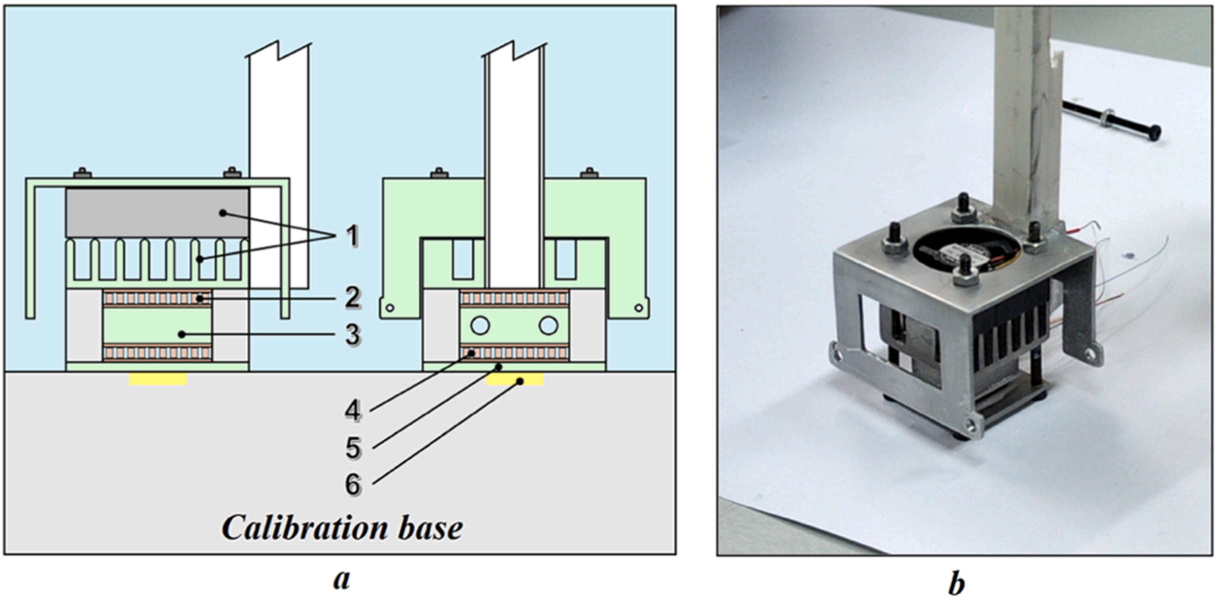

Fig. 1. Scheme (*a*) and picture (*b*) of the skin calorimeter. **1**: heatsink & fan, **2**: cooling thermopile, **3**: thermostat, **4**: measuring thermopile, **5** measuring plate, **6**: calibration element.

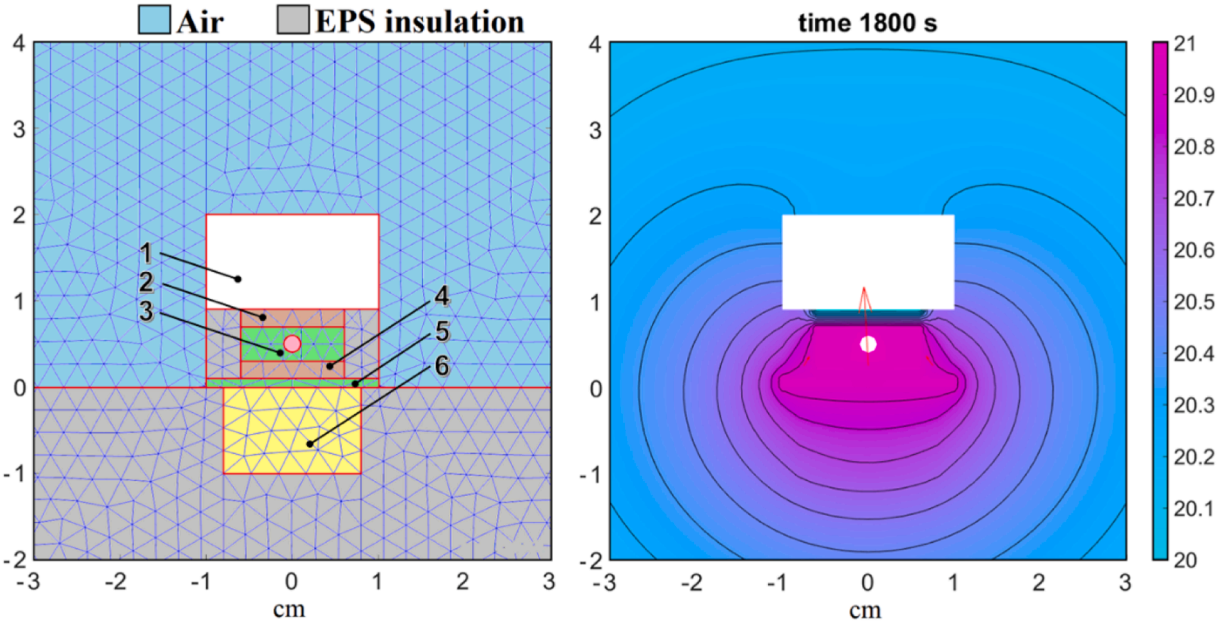

Fig. 2. **Left**: Skin calorimeter scheme and its surroundings, air, EPS base and sample. **1**: heatsink-fan, **2**: cooling thermopile, **3**: thermostat, **4**: measuring thermopile, **5** measuring plate, **6** sample. **Right**: Spatial distribution of temperatures for instant $t = 1800$s after a temperature jump of the thermostat from 20 to 21 °C.

introduction of boundary conditions and also allows the definition of a time variation of the thermostat's temperature. After that, we can obtain the time response of the temperatures at every point of the model. The section of the model is 15×15 cm^2, although Fig. 2 only shows the area near the sensor (6×6 cm^2). The domain triangulation used in the simulation is 1 mm.

The sample placed under the calorimeter (part **6** in Fig. 2) is prismatic, and its vertical thickness L will be modified in each simulation. The initial boundary condition will be an ambient temperature of 20 °C. The air domain is large enough to ensure this boundary condition. On the other hand, the calibration base is composed of an EPS block placed inside a steel box, so the lower temperature of the (steel) calibration base will be the ambient temperature of 20 °C. All simulations are similar: starting from a constant initial temperature of 20 °C in all elements, a thermostat temperature step from 20 °C to 21 °C is programmed. Fig. 2 (right) shows the spatial distribution of the temperatures for a time of 1800s measured from the instant at which the thermostat temperature step is programmed.

In the simulation we used the same samples that will be used in the experimental study. We have chosen yellow brass due to its high thermal conductivity and Teflon (PTFE), which is an insulating material that has thermal properties (heat capacity & thermal conductivity) comparable to skin (see Table 1).

Experimental tests showed that when enough pressure is applied, the thermal results are nearly identical with or without thermal paste. Furthermore, it is not practical to apply thermal paste to all samples, so

Table 1
Thermal properties of the materials used in the simulation.

	Density	*Conductivity*	*Heat capacity*	*Volumetric heat capacity*	*Thermal diffusivity*
	kg/m^3	W/mK	J/kg K	J/m^{3}K	m^2/s
Teflon (PTFE) [13]	2200	0.25	1000	2.2000×10^{6}	0.1136×10^{-6}
Steel [13]	7800	47	465	3.6270×10^{6}	12.9584×10^{-6}
Aluminum [13]	2700	237	900	2.4300×10^{6}	97.5309×10^{-6}
Alloy 3003[a] [14]	2730	193	893	2.4379×10^{6}	70.9167×10^{-6}
Yellow brass [13]	8410	116	380	1.1958×10^{6}	36.2976×10^{-6}
Human skin [15]	1109	0.37	3391	3.7606×10^{6}	0.0984×10^{-6}
Insulator EPS [16]	30	0.035	1450	0.0435×10^{6}	$0.8046\times10–^{6}$
Air[b]	1.155	0.025	1004	0.0012×10^{6}	21.5588×10^{-6}
Thermopile[c]	2937	1.26	647	1.9002×10^{6}	0.6631×10^{-6}

[a] Pure aluminum was used for the measuring plate, while alloy 3003 was used for the thermostat.

[b] Determined from altitude, atmospheric pressure, dew point and air temperature at laboratory normal conditions.

[c] Continuous-equivalent values calculated from the properties of its components, the thermal resistance value of the thermopile is obtained in the calorimeter Calibration and verify a good fit of these equivalent magnitudes.

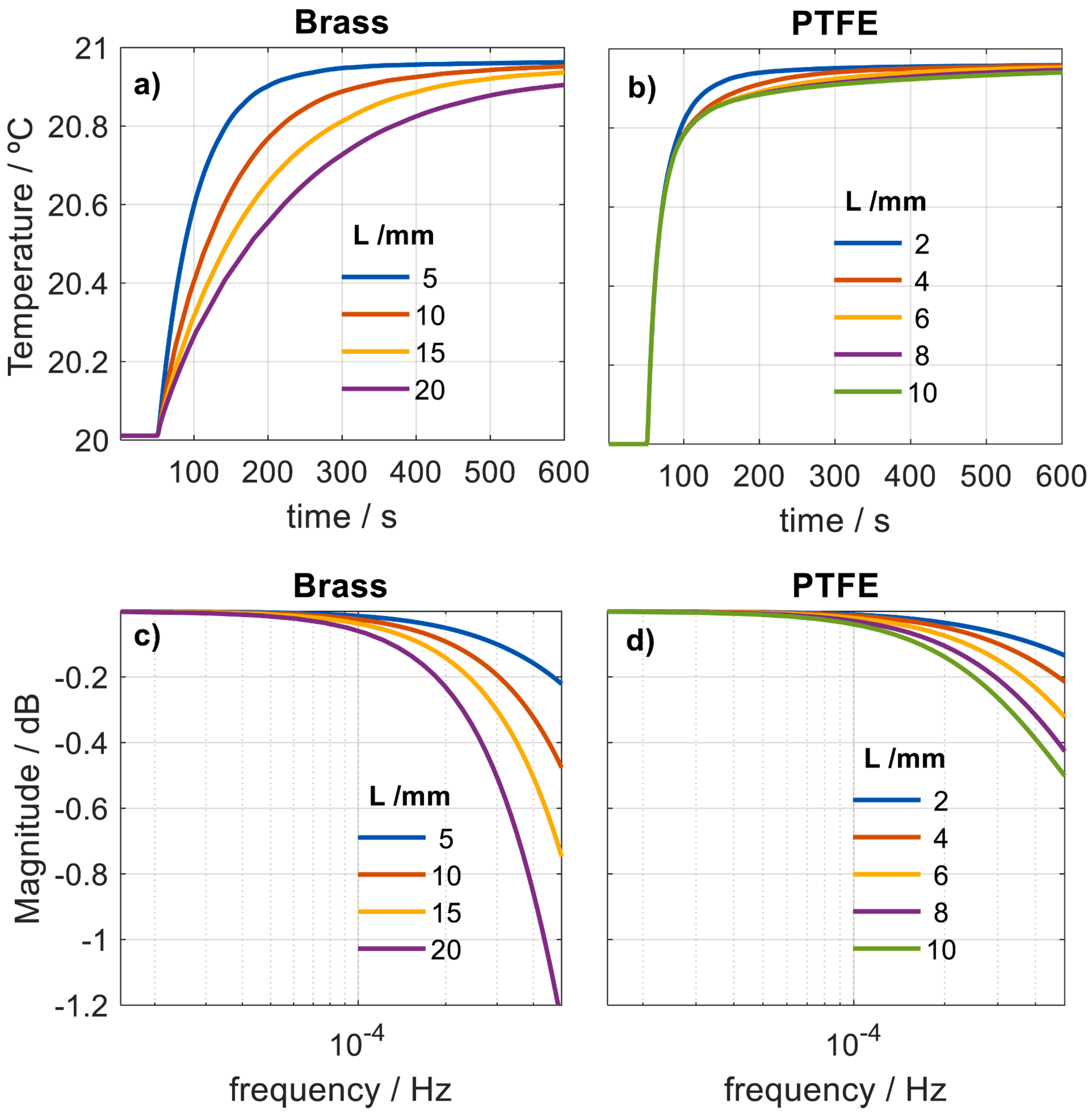

Fig. 3. Temperature of the measuring plate for a thermostat temperature input step of 20 to 21 °C, for prismatic samples of the same section and different thickness *L* & material (brass & PTFE). Frequency representation of the TF magnitude (2).

it was not used in the experiments. In this scenario, and considering the thermal contact between parts and the pressure applied [17], we assumed an air gap of 10 μm, a value which is consistent with both experimental and simulated results.

One of the purposes of the skin calorimeter is to determine the heat capacity of the sample under it. For this purpose, it is necessary to produce a temperature change and study the transient response. The temperature change is performed in the thermostat, so we consider a system of one input and one output, where the input is the temperature of the thermostat (T_{therm}) and the output is the temperature of the measuring plate (T_{plate}). Thus, we can define a Transfer Function, in the Fourier space, given by the expression (1):

$$TF(i\omega) = \frac{T_{output}(i\omega)}{T_{input}(i\omega)} = \frac{T_{plate}(i\omega)}{T_{therm}(i\omega)} \tag{1}$$

… where $\omega = 2\pi f$, f is the frequency in Hz. The input, in all simulated cases, will be a step signal from 20 to 21 °C. Fig. 3 shows the time responses for a brass sample of different thickness of $L = 5$, 10, 15 and 20 mm. The time responses for the case of a PTFE sample for thicknesses of $L = 2$, 4, 6, 8 and 10 mm are also shown.

As we can see in the time responses (Fig. 3), brass has a higher time constant than PTFE, due to its higher thermal diffusivity. In addition, as expected, the time constant increases as the size of the sample under the measuring plate increases. In PTFE case, above a certain thickness, time responses become indistinguishable. To better distinguish the dynamic responses in both cases, we have plotted the magnitude of the TF in dB:

$$\text{Magnitude}\,(dB) = 20\log_{10}\left|\frac{TF(i\omega)}{TF(0)}\right| \tag{2}$$

For the calculation of the TF($i\omega$), the baseline of the output signal is corrected, the time derivative is constructed and then the Fourier transform is calculated using the FFT (Fast Fourier Transform). Let's remember that the impulse response (response to a Dirac delta) is the time derivative of the response to a unit step.

In the next section, we will determine the parameters that define the TF for the proposed materials as a function of the sample size, which is determined by its thickness L. The goal is to explore a method that allows the determination of the heat capacity of the sample from the time response of the measuring plate temperature, when the temperature of the thermostat is changed. These two temperatures will determine the calorimetric signal given by the measurement thermopile.

4. Simple TFs and RC models

To propose a compact thermal model, it is first necessary to determine its size, i.e. the minimum number of elements in which the system can be modelled accurately reproducing its behavior. The size of the model can be determined by the number of poles of the TF that relates its input and output. In general, a TF can have N poles and M zeros ($N > M$) and its general expression, in Laplace space, will be (3):

$$TF(s) = \frac{T_{plate}(s)}{T_{therm}(s)} = K\frac{\prod_{i=1}^{M}(1+s\tau_i^*)}{\prod_{i=1}^{N}(1+s\tau_i)} \tag{3}$$

… where K is the sensitivity (response to a unit step input), and τ_i & $\tau_i{}^*$ are the inverses of the opposites of the poles (s_i) and zeros ($s_i{}^*$) of the TF ($\tau_i = -1/s_i$, $\tau_i{}^* = -1/s_i{}^*$). To identify the parameters of the TF we use an iterative method based on the Nelder-Mead algorithm [18–20]. For each group of TF parameter values (K, τ_i and $\tau_i{}^*$), the output signal, $T_{plate}(t)$, is reconstructed from the known input, $T_{therm}(t)$. This method recalculates the model parameters by minimizing a pre-established error criterion. The error criterion chosen is the Root Mean Square Error (RMSE) between the original signal and the one calculated with this model of poles and zeros (4):

$$\varepsilon = \frac{1}{np}\sqrt{\sum_{i=1}^{np}\left(T_{FEM}[i] - T_{TF}[i]\right)^2} \tag{4}$$

… where np is the number of points used in the fitting, T_{FEM} is the measurement plate temperature provided in the FEM simulation, and T_{TF} is the temperature calculated with the pole-zero model (TF model). This method, that consists of adjusting the parameters of the proposed models, will be used in all the cases developed below. That is, it will be used to determine the parameters of the TF model and the parameters of the RC model.

4.1. *Case of a heat conducting sample*

For heat-conducting materials such as yellow brass, we have found that a single-pole TF (one time constant) is enough to reconstruct the output signal, i.e. the input-output system can be modeled with a TF of the type (5):

$$TF(s) = \frac{T_{plate}(s)}{T_{therm}(s)} = \frac{K}{1+s\tau} \tag{5}$$

The brass samples analyzed have a constant cross section of 70.88 mm^2 (equivalent to a 9.5 mm diameter) and a thickness L in the direction of the sensor axis. Fig. 4 shows the FEM simulation curves and those obtained with the TF model for the cases of brass sample thickness $L =$ 10 mm and $L = 20$ mm. Fig. 4 also shows the values of sensitivity (K), time constant (τ) and RMSE (ε) committed with the TF model.

The identification of the model is acceptable with a single time constant. Therefore, a compact thermal model (RC model) of a single element connected to the thermostat is proposed (Fig. 5). This element, of heat capacity C_1, represents the sample and a part of the measuring plate. This domain is connected with the thermostat by a thermal conductance coupling P_{therm} and connected to the environment by a thermal conductance coupling P_1.

The equation that defines this RC model is the following (6):

$$0 = C_1\frac{dT_1}{dt} + P_{therm}(T_1 - T_{Therm}) + P_1(T_1 - T_{room}) \tag{6}$$

Correcting the baselines of all temperatures and applying the Laplace transform, we obtain the Transfer Function between the output (temperature of the measuring plate $T_1 = T_{plate}$) and the input (T_{therm}) (7):

$$TF(s) = \frac{T_1(s)}{T_{therm}(s)} = \frac{P_{therm}}{C_1 s + (P_1 + P_{therm})} \tag{7}$$

From the previous expression, the sensitivity (K) and the time constant (τ) can be deduced (8):

$$K = \frac{P_{therm}}{P_1 + P_{therm}};\ \tau = \frac{C_1}{P_1 + P_{therm}} \tag{8}$$

When a thermal perturbation is produced, the system's steady state will be reached at a time which is directly related with its time constants. However, when an experimental measurement is performed, the measurement time doesn't always coincide with the time needed to reach a full steady state. We define *measurement time* (t_m) as the time recorded from the start of the thermal perturbation until the end of the measurement. This time is relevant, since it indicates the time required to obtain an acceptable result of the thermal properties of the sample. Brass samples with different thickness (L) and measurement times (t_m) have been identified in Fig. 6.

We have determined the offset value of the heat capacity that can be identified by the model, $C_0 = 0.37$ J/K. In Fig. 6, the measurement times (t_m) are indicated for each heat capacity obtained (C_1). The continuous curves indicate the value of the offset heat capacity (C_0) plus the yellow brass sample heat capacity (C_{brass}). As we can see, up to 15 mm sample thickness, a measurement time of $t_m = 300$ s is enough to determine the

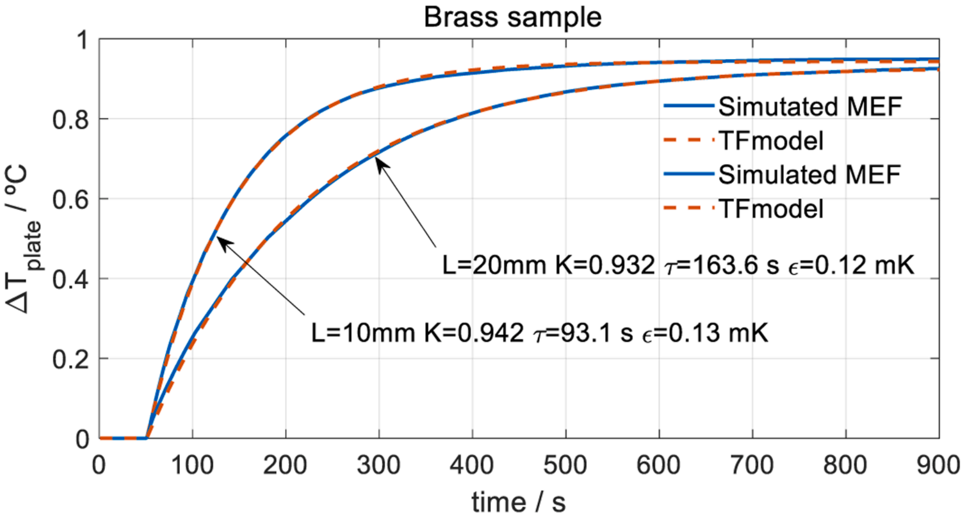

Fig. 4. Measuring plate temperature (ΔT_{plate}) fitting with a single-pole TF (5) for brass samples of $L = 10$ mm & 20 mm.

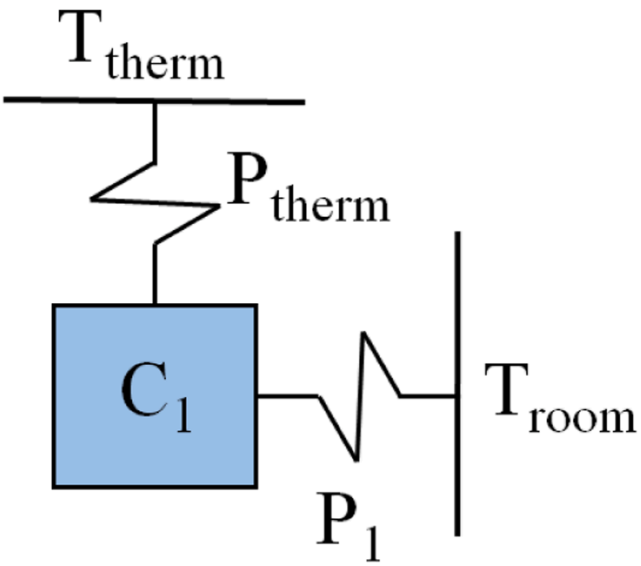

Fig. 5. RC Model scheme for heat conducting samples (yellow brass).

total sample heat capacity. However, for samples with a thickness $L > 15$ mm, a longer measurement time t_m is necessary to determine the correct heat capacity value. We can conclude that in the case of conducting materials, the thermal measurement depth is *complete* if measurement time t_m is enough. For the case studied, a measurement time $t_m = 1800$s is required for samples of $L > 15$ mm, & $t_m = 300$ s for samples of $L < 15$ mm. Fig. 6 also shows the values of the thermal conductance P_1 and the RMSE in the fittings. The conductance $P_{therm} = 23$ mW/K has been identified in this work as a constant value, since it represents the contact between the thermostat and the measuring plate. Note that this conductance includes the measuring thermopile and it was chosen as the constant value that best fits all the cases studied. Regarding the conductance P_1, it increases with the thickness of the sample as a result of the increasing lateral area of the sample.

4.2. Case of a heat insulating sample

The insulating material chosen in this study is a Teflon sample with different sizes. It has a constant cross section of 193.59 mm^2 (equivalent to a 15.7 mm diameter) and a thickness L. It is found that a one-time constant TF model is not enough to accurately reconstruct the measurement plate temperature T_{plate}. At least two time constants and an additional zero are necessary. The most suitable TF for this case is of the form (9):

$$TF(s) = \frac{T_{plate}(s)}{T_{therm}(s)} = \frac{K(1 + s\tau^{*})}{(1 + s\tau_1)(1 + s\tau_2)} \tag{9}$$

Fig. 7 shows the FEM simulation curves and those obtained with the TF model for the cases of Teflon sample thickness $L = 5$ mm and $L = 10$ mm. Fig. 7 also shows the values of the parameters of the TF (K, τ_1, τ_2, τ*) and the RMSE (ε) of the fitting.

Now, the model previously proposed in Eq. (6) is not valid, and a new two-element model is proposed. The first element represents the sample under the sensor and the second element represents the measuring plate connected with the thermostat, through the thermal coupling P_{therm} (Fig. 8).

The equations that define this model are the following (10):

$$\begin{aligned} 0 &= C_1\frac{dT_1}{dt} + P_{12}\left(T_1 - T_{plate}\right) + P_1\left(T_1 - T_{room}\right) \\ 0 &= C_{plate}\frac{dT_{plate}}{dt} + P_{therm}\left(T_{plate} - T_{therm}\right) + P_{12}\left(T_{plate} - T_1\right) + P_2\left(T_{plate} - T_{room}\right) \end{aligned} \tag{10}$$

Correcting the baselines of all temperatures (initially at room temperature), and applying the Laplace transform we obtain the TF (11):

$$\begin{aligned} TF(s) &= \frac{T_{plate}(s)}{T_{Therm}(s)} = \frac{(C_1 s + P_1 + P_{12})P_{therm}}{\Delta} \\ \Delta &= \begin{vmatrix} C_1 s + P_1 + P_{12} & -P_{12} \\ -P_{12} & C_{plate}s + P_2 + P_{12} + P_{therm} \end{vmatrix} \end{aligned} \tag{11}$$

This new proposed model has two poles which are the roots of the denominator determinant (Δ) and a zero (root of the numerator polynomial). This two-domain model is consistent with the one proposed in Eq. (9).

Fig. 9 shows the results of the T_{plate} curves fitting with the proposed RC model (Eqs. (10) and 11, Fig. 8). These results (heat capacity C_1, thermal conductances P_1 and P_{12}, and RMSE) are plotted as a function of the sample thickness L and the measurement time t_m. Previously, the invariant parameters, that do not depend on the thickness of the sample and the measurement time t_m, were determined. These parameters are, for PTFE, the offset heat capacity $C_0 = 0.14$ J/K, the heat capacity of the measuring plate $C_{plate} = 1.3$ J/K, and the thermal conductances $P_2 = 0.1$ mW/K & $P_{therm} = 74.4$ mW/K. The heat capacity plot (***a*** in Fig. 9) includes a solid green line that represents the true value of the sample heat

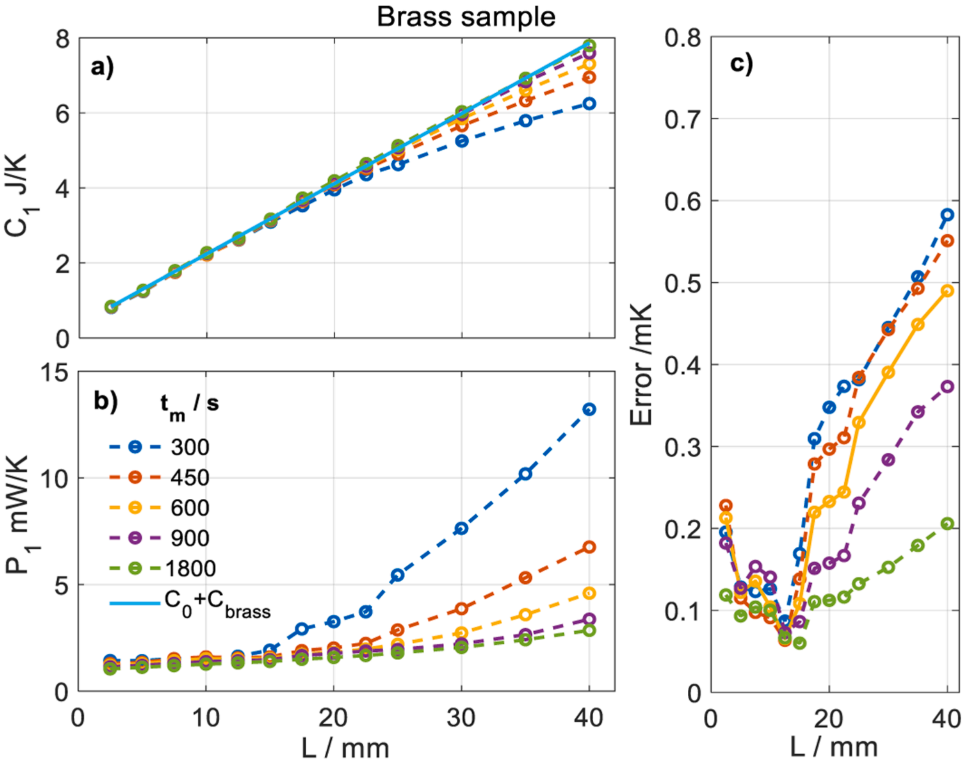

Fig. 6. *a)* heat capacity C_1 & *b)* thermal conductance P_1 of the RC Model (7) for heat conducting samples (yellow brass). Values obtained for different sample thickness & different measurement times t_m. *c)* RMSE (4).

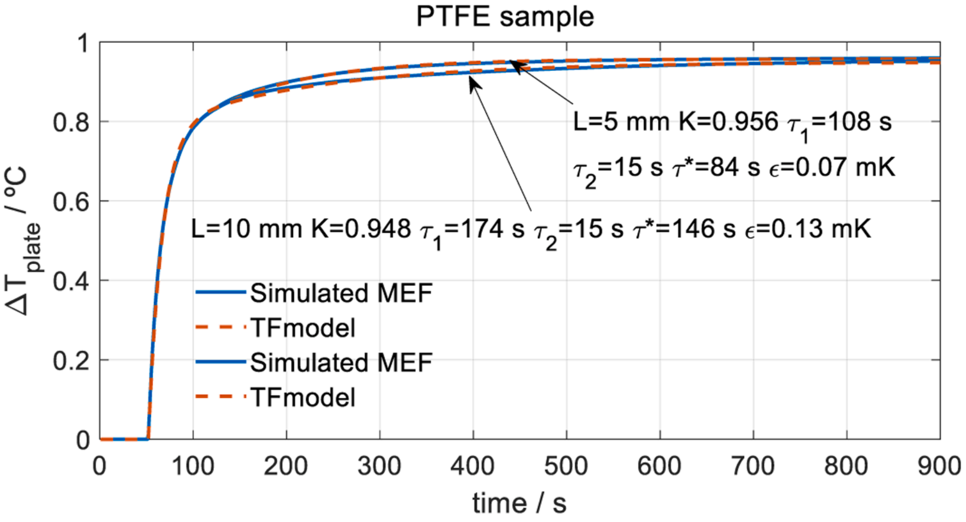

Fig. 7. Measuring plate temperature (ΔT_{plate}) fitting with a TF model (9) for Teflon samples of L = 5 mm & 10 mm.

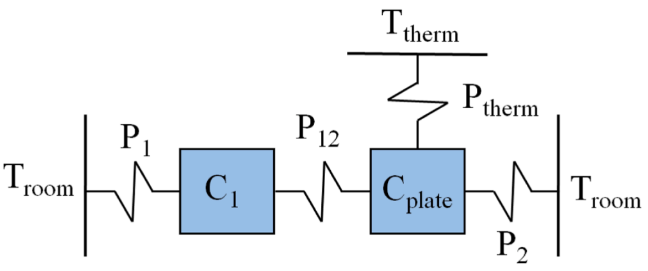

Fig. 8. RC Model scheme for the case of insulating samples (PTFE).

capacity plus the offset heat capacity $C_1 = C_0 + C_{PTFE}$. These results show that from a sample thickness $L > 5$ mm, it is not possible to obtain the heat capacity of the sample. We call this maximum thickness *thermal penetration depth* for this measurement time t_m. To reach a higher penetration (7.5 mm) it is necessary a higher measurement time t_m, at least one hour. We analyze the thermal penetration time dependence in the next section. On the other hand, the conductance P_1 increases slightly with sample thickness, because the lateral area of the sample increases. The conductance P_{12} decreases with sample thickness, because the distance between the geometrical centers between the two domains increases.

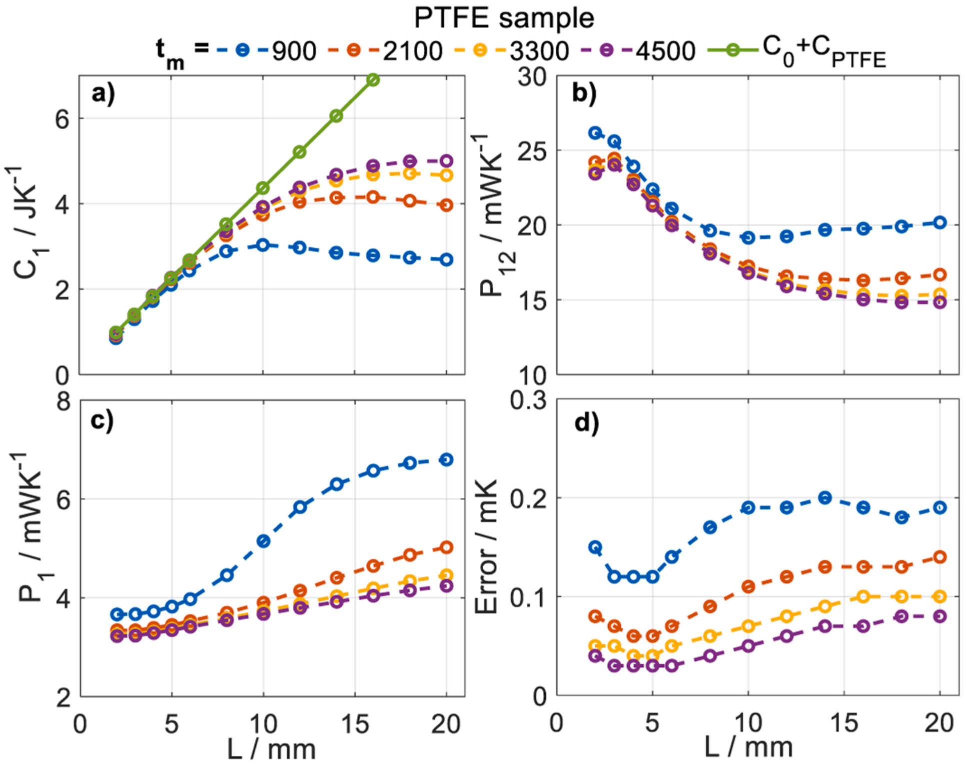

Fig. 9. Parameters *a)* C_1, *b)* P_{12} and *c)* P_1 of the RC Model (11) determined for different PTFE sample thickness and different measurement times t_m. The solid green line indicates the sum of the offset heat capacity plus the real sample heat capacity. *d)* RMSE (4).

5. Effect of time on the heat capacity measurement

In the previous section, heat capacity was plotted as a function of the sample thickness L and the measurement time t_m. We found that the measurement time t_m required depends on the sample thermal conductivity and its thickness. In this section, the dependence of the measured heat capacity on the measurement time t_m is studied in more detail. As said before, t_m is the time recorded from the start of the thermal perturbation until the end of the measurement. Fig. 10 shows the programmed temperature of the thermostat T_{therm} and its response on the measuring plate temperature, T_{plate}. The programmed rectangular pulses allow the determination of the sample's heat capacity during its heating

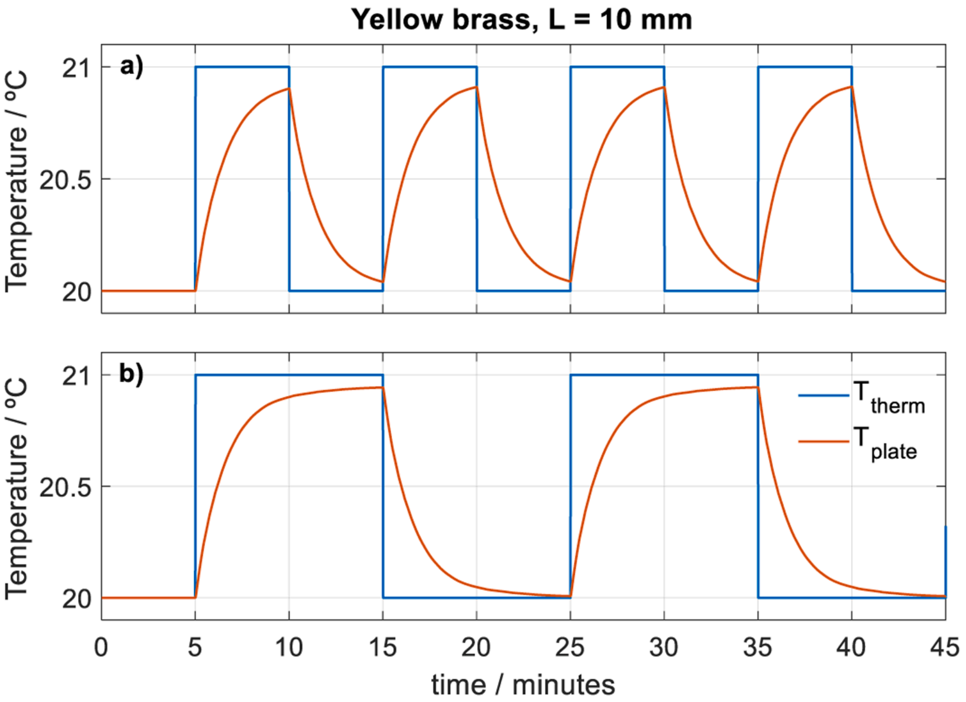

Fig. 10. Rectangular pulses of the thermostat temperature T_{therm} and temperature of the measuring plate T_{plate} for a brass sample (70.88 mm^2 area and L = 10 mm) for two different heating and cooling times (5 and 10 min).

and cooling. Fig. 10 shows the case of a 10 mm yellow brass sample with measurement times of $t_m = 5$ and 10 min. In this case, t_m coincides with the pulse duration.

Fig. 11 shows the heat capacity and the thermal conductance values obtained as a function of heating time for a brass sample. If the sample's thickness is longer than 20 mm, more time is required. For example, in the case of $L = 25$ mm, the variation of these properties is exponential, with a time constant of 4 min.

However, if the sample is an insulating material (PTFE), the thermal properties determined show a clear time dependence on t_m, and the time constants depend on the sample thickness (Fig. 12). Note that for a 5 mm sample the time constant is 7 min and for a 10 mm sample the time constant is 11 min. In the first case the heat capacity of the sample is correctly determined, but in the second case the nominal value is not reached, the obtained heat capacity is 3.9 J/K, and the real capacity is 4.2 J/K.

We briefly discuss the time variation of the thermal conductance P_1. Figs. 6 and 9 show that the value of P_1 increases with sample size, which is consistent with the C_1 increase. However, P_1 decreases exponentially with t_m since the temperature changes (Figs. 11 and 12). As the sample volume affected by the temperature change increases with t_m and the heat capacity C_1 increases, the conductivity P_1 also increases with the sample size affected, but its determination is simultaneously affected by the ambient temperature change, which results in a decrease in P_1. In an ideal case, the ambient temperature is considered to be constant, but in reality, this temperature (in the neighborhood of the calorimeter) varies with the thermostat's temperature change, which affects the evaluation of the conductivity P_1. When the baselines are corrected to the initial time, the term $P_1\ (T_1 - T_{room})$ in Eqs. (6) & (10), takes the form $P_1\ (\Delta T_1 - \Delta T_{room})$, where ΔT_{room} is the variation of the ambient temperature in the neighborhood of the calorimeter. This effect is reflected in a slight modification of P_1 to the value $P_1 \Delta T_{room}/\Delta T_1$. We have evaluated this quantity for the case of a PTFE sample of thickness from 2 to 8 mm, and there is approximately a 9% increase due to the increase in size and an 18% decrease due to the effect described above. This results in a final decrease of 11 %. This decrease is exponential because the heating of the environment and of the sample are also exponential. On the other hand, as already indicated above, there is a clear increase of P_1 with the thickness of the sample due to the increase of its lateral surface.

6. Effect of surface in the heat capacity measurement

We performed a detailed study of the determination of the RC model, for samples of constant area and different thicknesses, evaluating also the effect of the measurement time. However, when the skin calorimeter is applied on the human body surface, the skin area (sample) exceeds the sensing area of the sensor (4 cm^2). Therefore, it is necessary to study how the area of a low thermal conductivity sample (PTFE) affects the determination of the heat capacity. For this purpose, different areas (4, 5, 6, 8 and 10 cm^2) have been chosen.

The FEM simulations provide the temperature curves of the measuring plate as a function of time, and the RC model is determined from these curves. We consider the same constant parameters (C_{plate}, P_{therm} and P_2) as in the case described in Section 4.2. Figs. 13 and 14 show the calculated heat capacity C_1 of the sample, and the conductances P_1 and P_{12} between the sample and the surroundings (T_{room}) and with the neighbouring element (C_{plate}) according to Fig. 8. We note that for sample thicknesses of <4 mm, the heat capacities obtained are consistent with the nominal values of the sample. Regarding the sample surface, for an area of 5 cm^2 or more, the heat capacities determined are very similar (there is saturation). This results indicates a lateral limit in the determination of the heat capacity of the sample under the sensor.

On the other hand, the conductance P_1 increases with the area and with the thickness of the sample; and the conductance P_{12} decreases with the thickness of the sample. All this results are consistent with the results indicated in the previous sections. Regarding the effect of time, we can confirm the previous section discussion. As the sample thickness increases, more measuring time is required to determine the heat capacity of the sample. However, from a sample thickness over 4 mm, the nominal value of the heat capacity is not reached. For this thickness (4 mm), an area of 5 cm^2, and a measurement time of 1800s, the obtained heat capacity shows a difference with the nominal value of the sample of <5%. If the measurement time increases to 3600 s, the difference decreases to 4%. In conclusion, the measurement limits for this case would

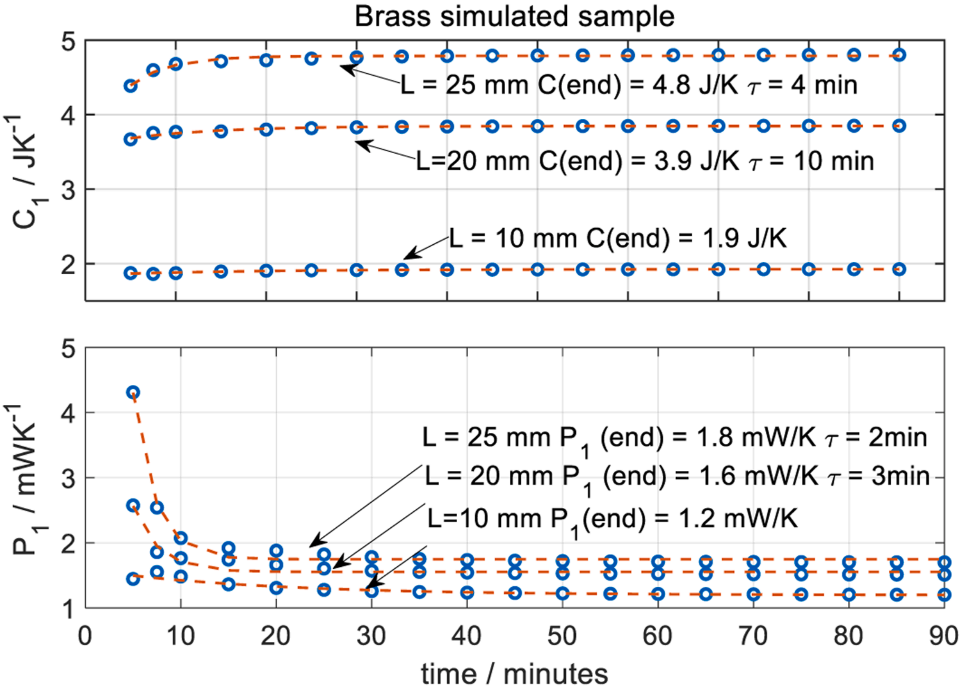

Fig. 11. Temporal representation of the RC Model parameters. Case of a brass sample of $L = 10$, 20 & 25 mm. The figure also shows the time constant τ of the exponential fit. C_0 offsets have been subtracted.

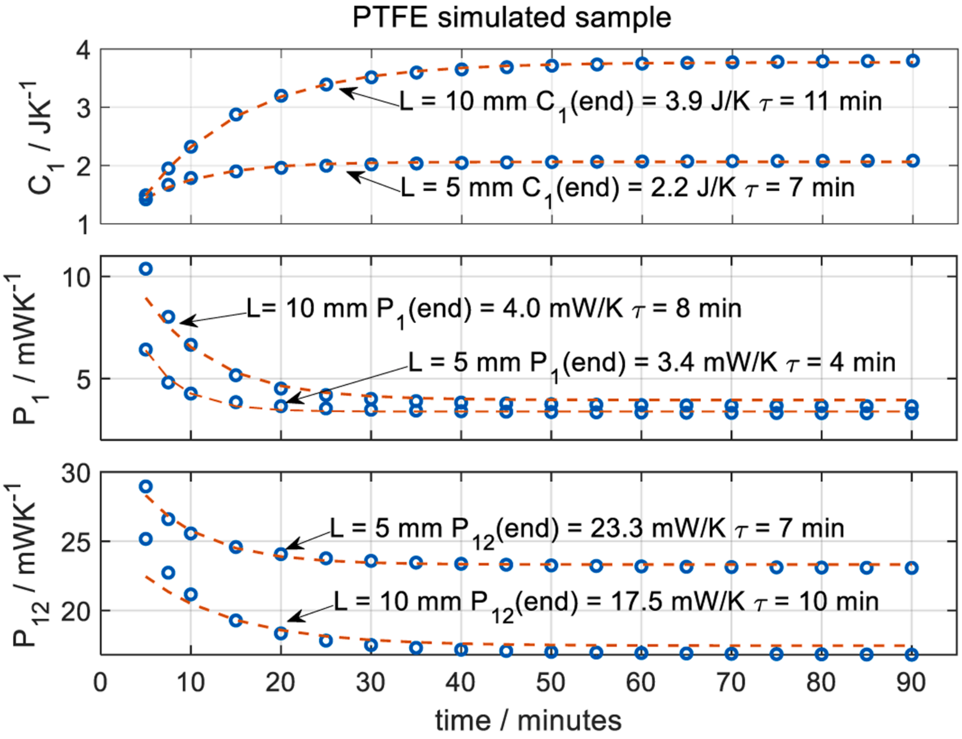

Fig. 12. Temporal representation of the RC Model parameters. Case of a PTFE sample of $L = 5$ & 10 mm. The figure also shows the time constant τ of the exponential fit. C_0 offset have been subtracted.

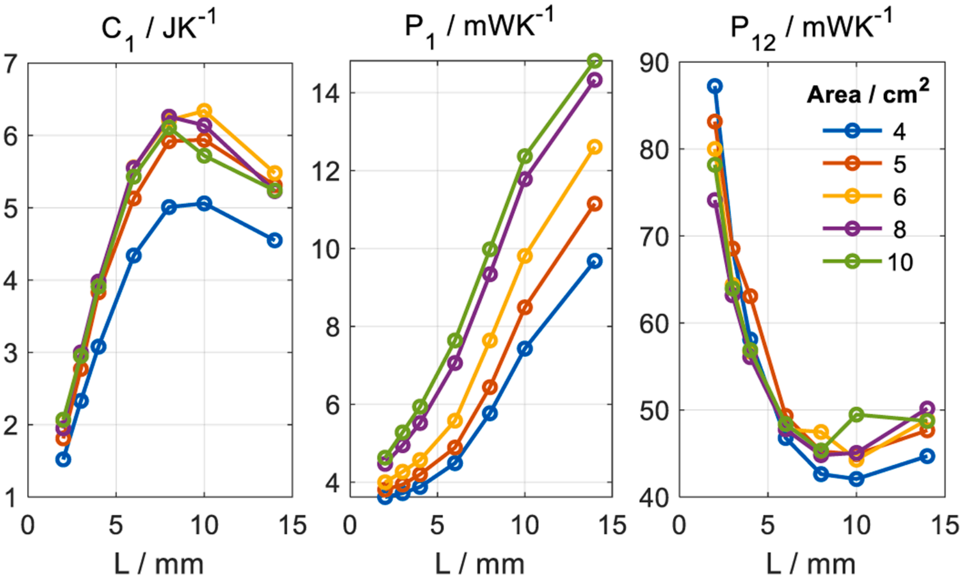

Fig. 13. Determined parameters of the RC model as a function of the PTFE sample area and thickness L, for a measurement time of 900 s.

be 4 mm thickness and 5 cm^2 area, and a measurement time after thermostat temperature change greater than 1800s.

7. Experimental study

In this case, it is necessary to develop an operating model that relates the calorimetric signal provided by the measuring thermopile (y) with the thermostat dissipated power (W_{therm}). Given the calorimetric signal-to-noise ratio, only two time constants can be identified. Therefore, a two-body model is proposed, as shown in Fig. 15:

The first element represents the measuring plate with the sample/skin/calibration block (parts 5 and 6 of Figs. 1 and 2). The second element represents the calorimeter's thermostat (part 3 of Figs. 1 and 2). These elements are connected to each other by the measuring thermopile, of thermal conductance P_{therm}. This thermopile provides the calorimetric signal $y(t) = k\ (T_1(t) - T_{therm}(t))$, where k is the Seebeck coefficient of the thermopile.

The model is based on the equations of heat transport by conduction, so the skin calorimeter can be considered as a two-input, two-output system. The first input is the power dissipated W_1 under the calorimeter's measuring plate, either in an electrical calibration or the heat dissipation of the skin area where the calorimeter is applied. The second

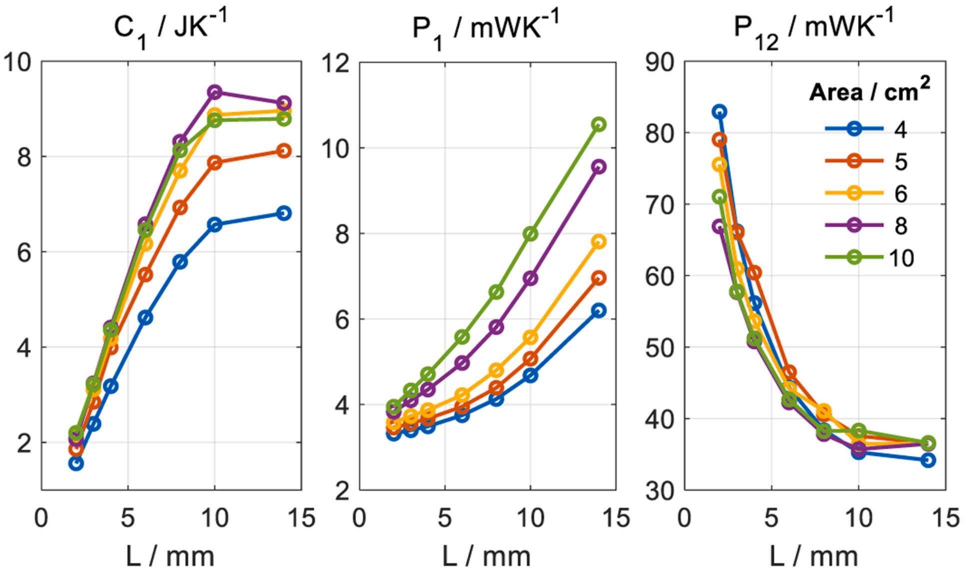

Fig. 14. Determined parameters of the RC model as a function of the PTFE sample area and thickness L, for a measurement time of 1800s.

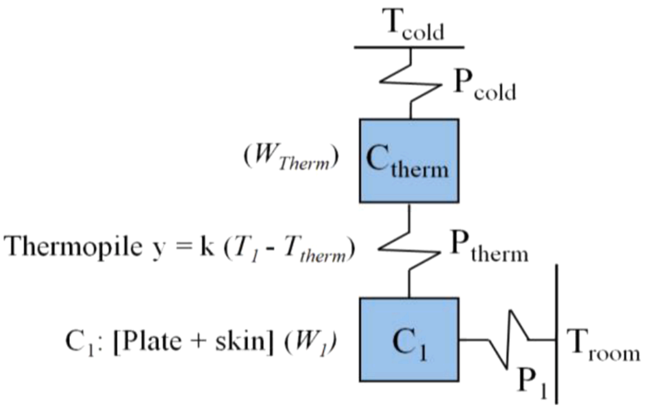

Fig. 15. RC Model of the skin calorimeter, used for experimental measurements.

input is the power W_2 dissipated by the thermostat to achieve the programmed temperature. The outputs are the calorimetric signal $y(t)$ and the thermostat temperature $T_{therm}(t)$. The model equations are as follows (12):

$$\begin{aligned} W_1 &= \frac{C_1}{k}\frac{dy}{dt} + \frac{P_1 + P_{therm}}{k}y + C_1\frac{dT_{therm}}{dt} + P_1(T_{therm} - T_0) \\ W_2 &= -\frac{P_{therm}}{k}y + C_{therm}\frac{dT_{therm}}{dt} + P_{cold}(T_{therm} - T_{cold}) \end{aligned} \tag{12}$$

…where T_0 is the room temperature around the sensor and T_{cold} the temperature on the cold side of the cooling thermopile. In the calorimeter's calibration, the model parameters are determined: heat capacities C_1 and C_{therm}, thermal conductances P_1, P_{cold} and P_{therm} and the constant of the measuring thermopile k. Of these parameters, only C_{therm}, P_{therm} and k can be considered invariant [9], since the others depend on the sample under the calorimeter, whether it is an inert sample or the skin of the human body. A previous work [9] explains the methodology used to determine the power dissipated by the skin and the thermal properties of the skin (heat capacity and thermal resistance). In this section we present the results of applying the calorimeter on inert samples and on the skin. Fig. 16 shows the calorimeter applied on air, to approximate the offset heat capacity $C_0 = 2.35$ J/K of the first domain (C_1), which is a sensor-specific parameter. Fig. 16 also shows the calorimeter on a Teflon sample and on the wrist of a healthy human subject.

In the same way as in the simulation, we now place the calorimeter on inert heat-conducting (brass) and insulating (PTFE) samples. Figs. 17 and 18 show the results obtained as a function of the time used for heating and cooling the sample (see Fig. 10). In the case of brass, we have used two cylinders of the same section (70.88 mm^2) but different mass ($m_1 = 5.27$ g and $m_2 = 12.50$ g). In the shorter cylinder the obtained heat capacity has no appreciable time dependence. However, in the case of the longer cylinder the value increases exponentially with measurement time t_m. The results obtained coincide with the real heat capacities of the samples.

For the case of an insulating material, a 10 mm PTFE sample has been used (see Fig. 16**b**), with a section of 193.59 mm^2. The heat capacity obtained (Fig. 18) increases exponentially with measurement time t_m and the final value obtained (1.6 J/K) after 60 min corresponds to a depth of approximately 4 mm. In other words, as the simulation had predicted, for these sample sizes, the nominal value of the sample can't be determined. We define the *thermal penetration depth* as the thickness of a sample with the same cross-section that would correspond to the experimentally obtained heat capacity. Generally, thermal penetration depth increases exponentially with time. D'Exposito et al. [21] performed a similar test in which they relate the thermal penetration depth with the frequency of a sinusoidal heating-cooling on SiGe HBT transistors. They found that the thermal penetration depth increases as frequency decreases.

Finally, Fig. 19 shows the results obtained in the wrist volar area of a healthy 65-year-old male subject. The results are qualitatively similar to PTFE with the difference that the skin has a higher volumetric heat capacity and a higher thermal conductance. If we consider a common skin heat capacity value [15], we obtain a depth of 2.6 mm. In this case the heat capacity variation has a lower time constant than in the case of PTFE, and after 45 min we obtain the final stationary value. It is clear that a measurement of this duration is not of practical application, but this study allows the estimation of the heat capacity that would be obtained for a given time. In the case shown, a 5-min application would provide a heat capacity of 2.87 J/K, equivalent to 1.9 mm depth.

8. Conclusions

A simulation study has been performed to analyze the characteristics of the heat capacity measurement of a skin calorimeter. In simulation, and experimentally, heat-conducting & insulating samples have been

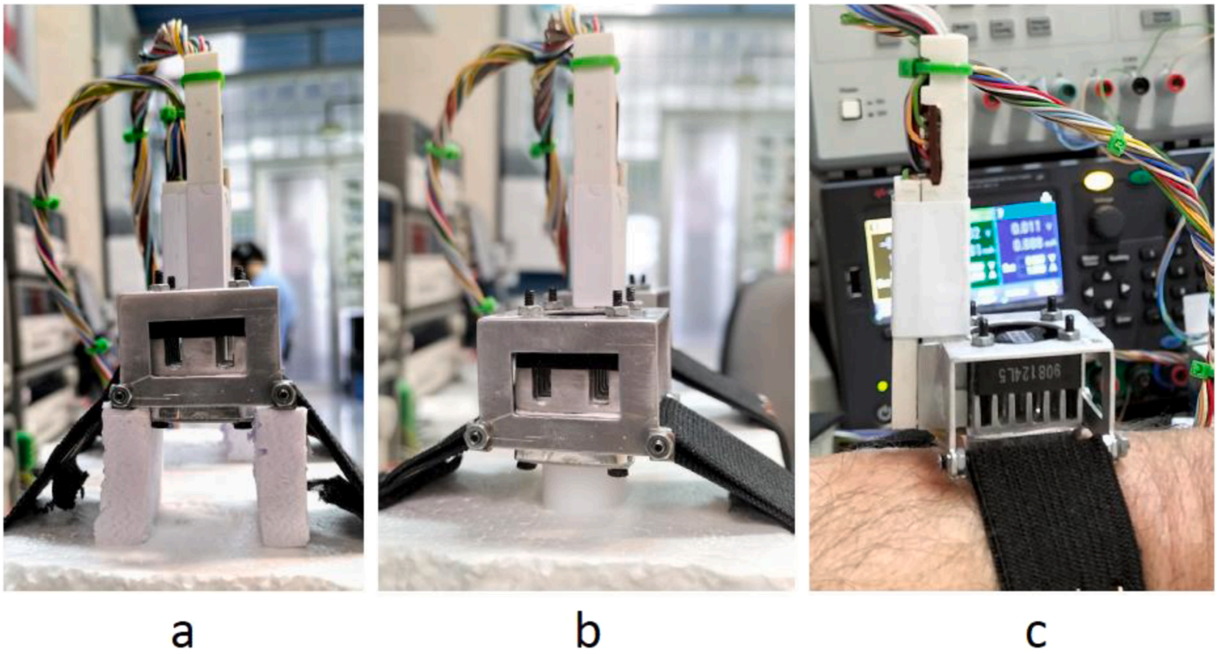

Fig. 16. Sensor applied on air (1), on PTFE (b) and on the wrist (c).

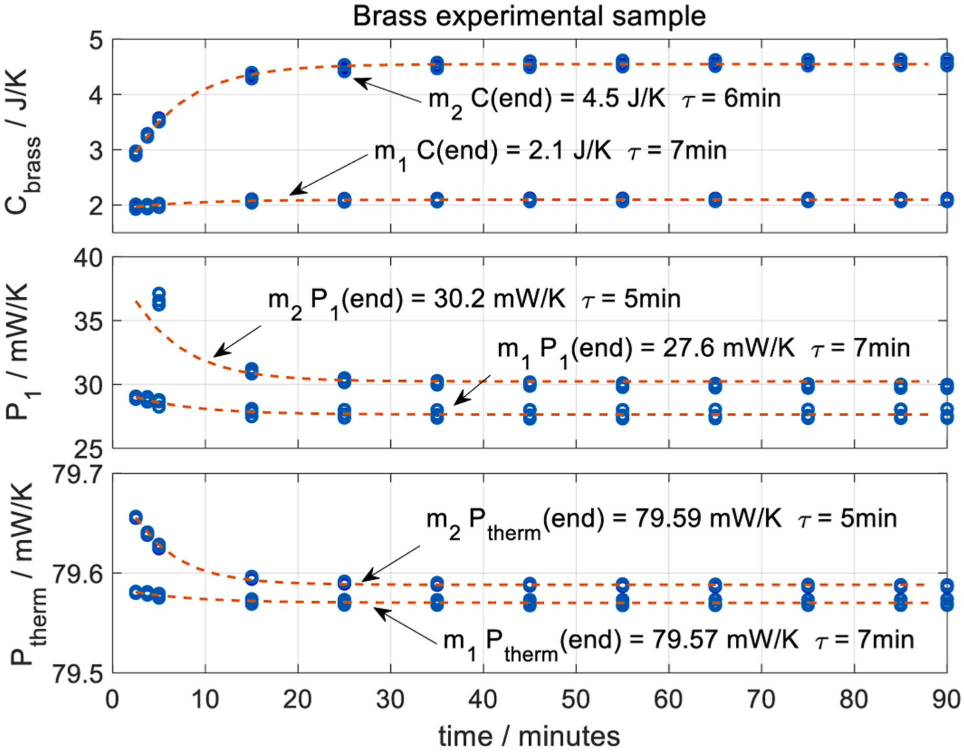

Fig. 17. Exponential fitting (dash lines) of C_{brass}, P_1 and P_{therm} from an experimental measurement. Case of two small brass rods of the same section (70.88 mm^2), but different masses ($m_1 = 5.27$ g and $m_2 = 12.50$ g). C_0 value has been subtracted. Real values, calculated from masses: 2.00 J/K for m_1 and 4.75 J/K for m_2.

considered (yellow brass & PTFE). Experimental measurements have also been performed on the skin. We conclude that:

1. **FEM simulation** is a good tool to reproduce the skin calorimeter's behavior for different inputs and materials, and the proposed RC modeling allows the accurate determination of the heat capacity of the sample under the sensor. The modeling also allows to study the limitations and operating ranges of the instrument.
2. **For the case of heat-conducting materials**, with a short measurement it is possible to determine the full heat capacity of a sample (300 s is enough for samples of 71 mm^2 & $L < 15$ mm), although this has a limit (for samples $L > 15$ mm is required more time to measure the full heat capacity). In addition, these results show a new potential application for this instrument. Although the skin calorimeter was designed to measure on the skin, it is also able to determine the heat capacity of small heat-conducting parts.

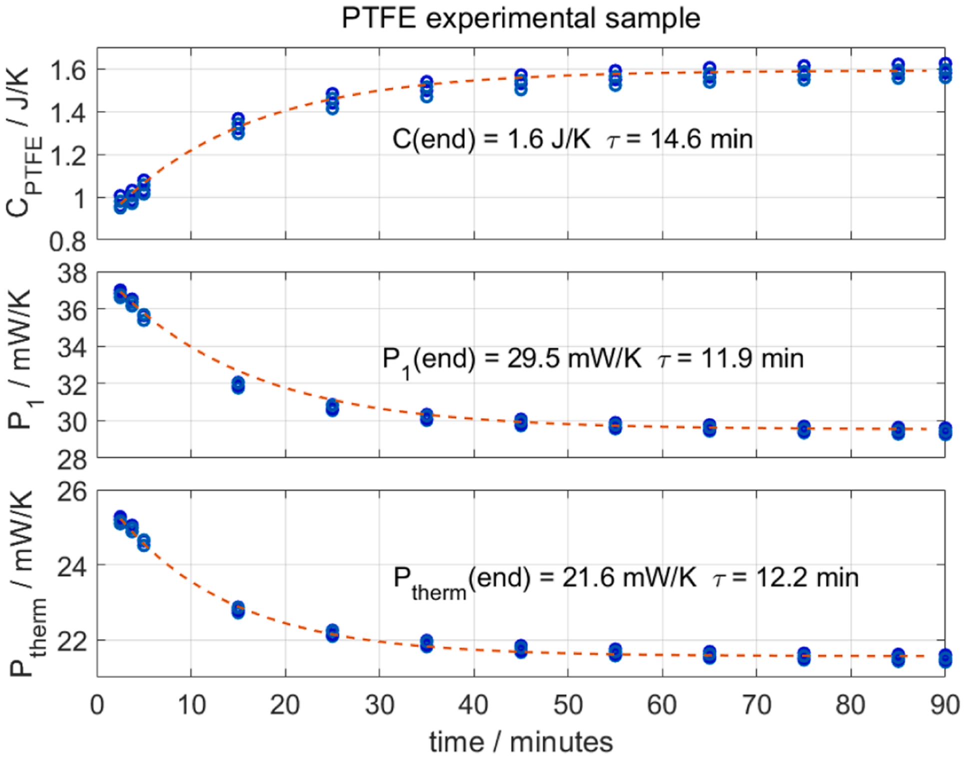

Fig. 18. Experimental measurement result for PTFE. In this case the thermal penetration depth is 4.3 mm, the sample thickness is 10 mm and the section 193.59 mm^2.

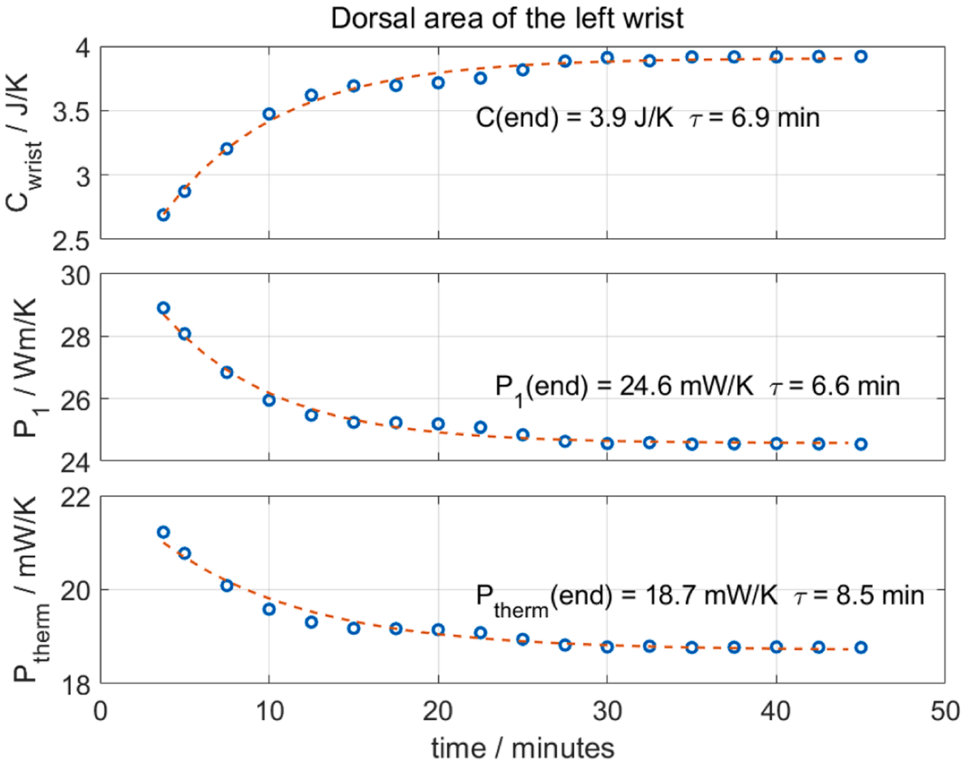

Fig. 19. Measurement in the left wrist dorsal area of a healthy 66-year-old male.

Experimentally, yellow brass cylinders with similar volumes to the simulation ones have been used (71 mm^2 and 10 – 20 mm thickness). An accurate measurement of the sample's heat capacity has been obtained (95 % of the real value). The dependence of the result on the measurement time has been verified.

3. **For the case of heat-insulating materials**, the measurement presents several difficulties. For small samples, (194 mm^2 & $L < 5$ mm),

a minimum measurement time of 900 s is required to determine the full heat capacity of the sample. However, above five millimeters sample thickness, the results begin to diverge. For example, for a sample of 7.5 mm thickness, a measurement time of >3600 s is required to approach the full heat capacity of the sample.

Experimentally, a PTFE cylinder of the same section & $L = 10$ mm has been used. The results obtained show that the instrument is able to measure a maximum heat capacity after 60 min of measurement of 1.6 J/K, which would correspond to a 4 mm thickness sample. This limitation in the heat capacity measurement defines the thermal penetration depth of the instrument, that depends on time, but has a final max value.

The skin has thermal properties comparable to PTFE. Thus, the instrument is potentially able to measure the thermal properties of the skin with a penetration comparable to PTFE (4 mm). Experimentally, this penetration is (in the case of the wrist – is important to mention that every part of the human skin may behave differently –) of 1.9 – 2.6 mm.

CRediT authorship contribution statement

Pedro Jesús Rodríguez de Rivera: Writing – review & editing, Writing – original draft, Validation, Supervision, Software, Methodology, Investigation, Data curation, Conceptualization. **Miriam Rodríguez de Rivera:** Writing – review & editing, Visualization, Supervision, Methodology, Investigation, Formal analysis, Data curation. **Fabiola Socorro:** Writing – review & editing, Validation, Supervision, Software, Investigation, Formal analysis, Conceptualization. **Manuel Rodríguez de Rivera:** Writing – review & editing, Writing – original draft, Validation, Supervision, Software, Resources, Methodology, Investigation, Formal analysis, Conceptualization.

Declaration of competing interest

The authors declare that they have no known competing financial interests or personal relationships that could have appeared to influence the work reported in this paper.

Data availability

Data will be made available on request.

Funding

This research did not receive any specific grant from funding agencies in the public, commercial, or not-for-profit sectors.

References

[1] W. Uwe, W. Frenz, V. Rumpler, Correcting heat storage in a calorimetric chamber by a two-compartment-model, Thermochim. Acta 292 (1997) 1–2, https://doi.org/10.1016/S0040-6031(97)00035-X, 1-7.

[2] R.A. Robergs, A critical review of the history of low- to moderate-intensity steady-state VO_2 kinetics, Sport. Med. 44 (2014) 641–653, https://doi.org/10.1007/s40279-014-0161-2.

[3] P.J. Rodríguez de Rivera, Mi Rodríguez de Rivera, F. Socorro, M. Rodríguez de Rivera, Heat flow measurement of human skin using a calorimetric sensor with a programmable thermostat. An alternative to climate chambers, Measurement 201 (2022) 111693, https://doi.org/10.1016/j.measurement.2022.111693.

[4] https://www.hukseflux.com/Accessed on April 2024.

[5] X. Zhang, C. Bontozoglou, P. Xiao, In vivo skin characterizations by using opto-thermal depth-resolved detection spectra, Cosmetics 6 (2019) 54, https://doi.org/10.3390/cosmetics6030054.

[6] T. Okabe, T. Fujimura, J. Okajima, S. Aiba, S. Maruyama, Non-invasive measurement of effective thermal conductivity of human skin with a guard-heated thermistor probe, Int. J. Heat Mass Transf. 126 (2018) 625–635. http://doi.org/10.1016/j.ijheatmasstransfer.2018.06.039.

[7] P.J. Rodríguez de Rivera, Mi Rodríguez de Rivera, F. Socorro, M. Rodríguez de Rivera, Validation of a skin calorimeter to determine the heat capacity and the thermal resistance of the skin, Sensors 23 (2023) 4391, https://doi.org/10.3390/s23094391.

[8] P.J. Rodríguez de Rivera, Mi Rodríguez de Rivera, F. Socorro, M. Rodríguez de Rivera, Monitoring of some minor human skin lesions using a skin calorimeter, J Therm. Anal. Calorim. (2024), https://doi.org/10.1007/s10973-024-13204-6.

[9] P.J. Rodríguez de Rivera, Mi Rodríguez de Rivera, F. Socorro, M. Rodríguez de Rivera, Experimental study of the thermal probing depth of a skin calorimeter, Int. J. Heat Mass Transf. 212 (2023) 124258, https://doi.org/10.1016/j.ijheatmasstransfer.2023.124258.

[10] H.S. Carslaw, J.C. Jaeger, Conduction of Heat in Solids, Oxford at the Clarendon Press, London, 1959.

[11] Y. Lifen, Y. Jianlin, Q. Suxin, Revisiting thermal penetration depth for caloric cooling system, Appl. Therm. Eng. 178 (2020) 115605, https://doi.org/10.1016/j.applthermaleng.2020.115605.

[12] https://es.mathworks.com/help/pdf_doc/pde/index.html. Accessed on April 2024.

[13] https://www.goodfellow.com/Accessed, on April 2024.

[14] https://www.americanelements.com/aluminum-3003-alloy Accessed, on September 2024.

[15] P.A. Hasgall, F. Di Gennaro, et al., IT'IS Data Base for Thermal and Electromagnetic Parameters of Biological Tissues, Version 4.1, Feb 22, 2022, https://doi.org/10.13099/VIP21000-04-1.

[16] k. Maatouk, a. Shaimaa, h. Ahmed, d. Abeer, Impact of dynamic thermal conductivity change of EPS insulation on temperature variation through a wall assembly, Case Stud. Therm. Eng. 25 (2021) 100917, https://doi.org/10.1016/j.csite.2021.100917.

[17] *Thermal contact resistance*. A to Z of Thermodyn.. https://doi.org/10.1615/AtoZ.t.thermal_contact_resistance. Accessed, on September 2024.

[18] J.A. Nelder, C. Mead, A simplex method for function minimization, Comput. J. 7 (1965) 308–313, https://doi.org/10.1093/comjnl/7.4.308.

[19] J.C. Lagarias, J.A. Reeds, M.H. Wright, P.E. Wright, C*onvergence properties of the Nelder-Mead simplex method in low dimensions*, SIAM J. Optim. 9 (1) (1998) 112–147, https://doi.org/10.1137/S1052623496303470.

[20] https://es.mathworks.com/help/matlab/ref/fminsearch.html Accessed, on April 2024.

[21] R. D'Esposito, S. Balanethiram, J.L. Battaglia, S. Frégonèse, T Zimmer, Thermal penetration depth analysis and impact of the BEOL metals on the thermal impedance of SiGe HBTs, IEEE Electron. Dev. Lett. 38 (10) (2017) 1457–1460, https://doi.org/10.1109/LED.2017.2743043.